Aero-Propulsive Damping Characterization for eVTOL Aircraft Using Free Motion Wind-Tunnel Testing

Benjamin M. Simmons,* Kasey A. Ackerman,[†] and Garrett D. Asper[‡]
NASA Langley Research Center, Hampton, Virginia 23681

This paper describes an electric vertical takeoff and landing (eVTOL) aircraft system identification method applied using three degree-of-freedom (3DOF) free motion wind-tunnel testing. The approach, similar to flight-test system identification, allows for efficient mathematical model development of the aero-propulsive moments applied on an eVTOL vehicle, including aerodynamic damping effects. The approach is demonstrated using a subscale tiltrotor eVTOL aircraft mounted on a new 3DOF wind-tunnel apparatus. To execute the test, a model-based 3DOF control system is designed to track attitude commands and transition the aircraft based on the freestream dynamic pressure. While the flight controller is active, orthogonal phase-optimized multisine inputs are injected into the attitude command and control effector command signals to enable collection of informative data for model identification. Aero-propulsive models are then identified at several reference conditions in the transition flight envelope using the equation-error method in the frequency domain. The identified models are shown to have a good fit to the modeling data and good prediction capability of data not used for model identification. The method yields aerodynamic damping estimates using less wind-tunnel test time compared to traditional forced oscillation experiments and supplements static wind-tunnel testing to produce a comprehensive transition aero-propulsive model suitable for use in flight dynamics simulations.

Nomenclature

g	=	gravitational acceleration, ft/s^2
I_x, I_y, I_z, I_{xz}	=	aircraft inertia tensor elements, slug·ft^2
L, M, N	=	body-axis aero-propulsive rolling, pitching, and yawing moment, ft·lbf
m	=	aircraft mass, slug
$n_1, n_2,..., n_6$	=	proprotor rotational speeds, rev/s
p, q, r	=	body-axis angular velocity components, rad/s or deg/s
$\bar{q} = \frac{1}{2}\rho V^2$	=	freestream dynamic pressure, lbf/ft^2
u, v, w	=	body-axis translational velocity components, ft/s
V	=	freestream velocity, ft/s
X, Y, Z	=	body-axis aero-propulsive forces, lbf
α	=	angle of attack, rad or deg
β	=	angle of sideslip, rad or deg
$\delta_{c_1}, \delta_{c_2},..., \delta_{c_6}$	=	collective pitch angles, rad or deg
$\delta_{f_1}, \delta_{f_2},..., \delta_{f_6}$	=	flaperon deflection angles, rad or deg
$\delta_{t_1}, \delta_{t_2}, \delta_{t_3}, \delta_{t_4}$	=	nacelle tilt angles, rad or deg
δ_r	=	rudder deflection angle, rad or deg
δ_s	=	stabilator deflection angle, rad or deg
ϕ, θ, ψ	=	Euler roll, pitch, and yaw angles, rad or deg
ρ	=	air density, slug/ft^3

Superscripts

T	=	transpose
-1	=	matrix inverse
$\hat{}$	=	estimate
$\dot{}$	=	time derivative
$\bar{}$	=	mean
$\tilde{}$	=	Fourier transform
$\dagger$	=	complex conjugate transpose

---

*Research Aerospace Engineer, Flight Dynamics Branch, Member AIAA.
[†]Research Aerospace Engineer, Dynamic Systems and Control Branch, Member AIAA.
[‡]Pathways Intern, Flight Dynamics Branch, Student Member AIAA.

I. Introduction

Recent technology advances have helped to enable practical electric vertical takeoff and landing (eVTOL) aircraft for Advanced Air Mobility (AAM) applications. eVTOL vehicles are suited for a variety of missions, including crewed vehicles such as air taxis or emergency response vehicles, as well as uncrewed vehicles for package delivery, cargo transportation, surveillance, and atmospheric sensing applications, among others. These novel vehicles can be considered a new class of aircraft that have features of both traditional fixed-wing and rotary-wing aircraft, as well as new attributes such as distributed electric propulsion (DEP). eVTOL aircraft have the ability to operate efficiently at high speeds similar to fixed-wing aircraft, while also being able to takeoff and land vertically and precisely maneuver in confined urban areas like rotary-wing aircraft. The use of DEP technology has significantly expanded the transitional aeronautical vehicle design space and has resulted in a multitude of unique vehicle configurations [1–5]. As of November 2024, Ref. [6] reports that over 1000 different eVTOL aircraft concepts have been developed, including tiltwing, tiltrotor, lift+cruise, and multirotor configurations.

Although eVTOL vehicles have promising capabilities, there are still numerous research challenges that need to be addressed before widespread operational use of these new aircraft is enabled, such as flight control system development, air traffic management, handling qualities, contingency management, and autonomy. A common multidisciplinary need for many research areas is a flight dynamics simulation driven by high-fidelity aero-propulsive models; however, efficient and accurate model development is challenged by significant aero-propulsive coupling, many independent control effectors, vehicle instability, and rapidly changing aerodynamics and control effectiveness through transition. Previous research has investigated methods for efficient, empirical eVTOL aircraft aero-propulsive modeling across their wide flight envelopes using wind-tunnel testing [7–12]. Other work has applied similar methods to CFD experiments [13, 14] and simulated flight testing [15]. Based on these studies, Refs. [10, 11, 14] justified the use of eVTOL-aircraft-specific modeling procedures, building on established fixed-wing and rotary-wing aircraft system identification methods [16–18]. Efficient dynamic control input design for modeling eVTOL aircraft is discussed in a wind-tunnel and flight-test context in Refs. [11, 15].

Several static wind-tunnel tests have occurred for eVTOL aircraft [7–12, 19], but wind-tunnel testing with dynamic vehicle motion has not yet received much focus. Common dynamic wind-tunnel testing approaches include forced oscillation, rotary balance, free motion in certain degrees of freedom (e.g., free-to-roll), and free flight [20]. Forced oscillation and rotary balance mechanisms prescribe the motion of a wind-tunnel model while forces and moments on the vehicle are measured. Forced oscillation experiments are a common way to determine aerodynamic damping derivatives [21–23]. In contrast to forced motion techniques, free motion and free flight techniques generally use active effectors to control aircraft motion. Wind-tunnel apparatuses that allow free motion in one or more degrees of freedom have taken numerous forms over the past few decades [24]. References [25–29] provide examples of single degree-of-freedom (DOF) wind-tunnel experiments. Multiple DOF wind-tunnel testing efforts have included 2DOF [30–32], 3DOF [33, 34], 4DOF [35, 36], and 5DOF [37–39] experiments. Wind-tunnel studies that employ single or multiple DOF test rigs allow for both estimation of dynamic models and evaluation of inner-loop flight control algorithms.

Building on previous eVTOL aircraft modeling research and free motion wind-tunnel test techniques, the present work uses a new three degree-of-freedom (3DOF) wind-tunnel apparatus and system identification techniques to develop a dynamic aero-propulsive model for a subscale eVTOL aircraft. Multisine maneuvers that perturb the aircraft around trimmed flight conditions are executed throughout the transition envelope, and modeling is performed using the equation-error method in the frequency domain at each reference condition in post-test analysis. The input design and parameter estimation methods used for this work were adapted from the System IDentification Programs for AirCraft (SIDPAC) software toolbox [16, 40]. Although multiple DOF wind-tunnel testing has been used for numerous applications for fixed-wing aircraft, to the best knowledge of the authors, this paper presents the first application of multiple DOF wind-tunnel testing to eVTOL aircraft.

The paper is organized as follows: Section II introduces the experimental aircraft. Section III gives an overview of previous static wind-tunnel testing and aero-propulsive model efforts, which enabled development of a model-based flight control system outlined in Sec. IV. Section V presents the experiment design used to collect data for model identification, followed by a description of the wind-tunnel testing approach in Sec. VI and modeling strategy in Sec. VII. Section VIII provides sample local and global modeling results, leading into a discussion of the results and modeling approach in Sec. IX. Overall conclusions are summarized in Sec. X.

II. Aircraft

The wind-tunnel testing and modeling approaches demonstrated in this paper were applied to the Research Aircraft for eVTOL Enabling techNologies (RAVEN) Subscale Wind-Tunnel and Flight Test (SWFT) model built at NASA Langley Research Center (LaRC) [41]. The RAVEN-SWFT is a 28.6% scale version of the RAVEN 1000-lb class eVTOL aircraft concept [42], which has been designed in a collaborative effort between NASA LaRC and the Georgia Institute of Technology (Georgia Tech). The RAVEN aircraft is a tiltrotor eVTOL configuration with six variable-pitch proprotors. The front four proprotors tilt forward and are operational throughout the entire flight envelope. The rear two proprotors do not tilt and serve as lifting proprotors in hover and transition. The aircraft control surfaces include six flaperons, a stabilator, and a rudder. In total, the vehicle has 24 independent control effectors:

- Six proprotor rotational speeds ($n_1, n_2, ..., n_6$)
- Six proprotor collective pitch angles ($\delta_{c_1}, \delta_{c_2}, ..., \delta_{c_6}$)
- Four nacelle tilt angles ($\delta_{t_1}, \delta_{t_2}, \delta_{t_3}, \delta_{t_4}$)
- Six flaperon deflection angles ($\delta_{f_1}, \delta_{f_2}, ..., \delta_{f_6}$)
- One stabilator deflection angle (δ_s)
- One rudder deflection angle (δ_r)

Figure 1 shows a schematic of the RAVEN aircraft with annotations showing the vehicle propulsor and control surface definitions. Flaperon and stabilator deflections are defined as positive trailing edge down. Rudder deflection is defined as positive trailing edge left. Nacelle tilt angle settings of 0 deg correspond to the horizontal, forward flight position; nacelle tilt angle settings of 90 deg correspond to the vertical position used near hover. As currently configured, proprotor 1, 3, and 5 rotate counterclockwise and proprotor 2, 4, and 6 rotate clockwise, as viewed from the perspective of each electric motor located behind its respective proprotor.
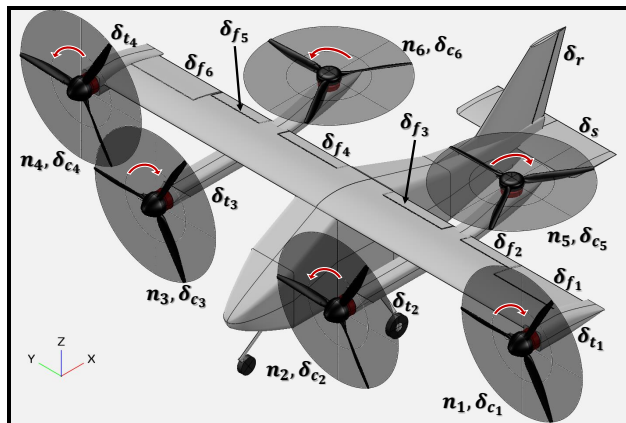

Fig. 1   RAVEN control effector definitions.

Table 1   RAVEN-SWFT inertia tensor elements

Property	Value	Units
I_x	2.169	slug·ft^2
I_y	0.897	slug·ft^2
I_z	2.551	slug·ft^2
I_{xz}	0.0046	slug·ft^2

The RAVEN-SWFT, pictured in the NASA Langley 12-Foot Low-Speed Tunnel (LST) [43] in Fig. 2, was designed as a flight dynamics and controls research testbed to advance eVTOL aircraft technology. As its name suggests, the vehicle is designed for use in both wind-tunnel and flight-test experiments. The aircraft has a projected flight weight of 38 pounds, a wingspan of 5.7 ft (excluding the outboard tilt nacelles), and a proprotor diameter of 19.5 inches. The current hover and forward flight estimates of the RAVEN-SWFT moments of inertia and product of inertia, experimentally determined using both torsional and compound pendulum methods, are provided in Ref. [41]. For this work, the inertia tensor, given in Table 1, is assumed to be constant across the flight envelope and its elements are taken to be the average of the hover and cruise inertia tensor values. This is justifiable because the diagonal elements of the hover and forward flight inertia tensor have a percent difference of less than 1%, which is less than the predicted uncertainty in the estimates.

The RAVEN-SWFT was developed at NASA LaRC as one of several subscale eVTOL research aircraft intended to explore their unique flight characteristics and resolve implementation challenges to help bring similar full-scale vehicles into mainstream operation. Previous aircraft have included the LA-8 [44, 45] and GL-10 [46], which have enabled research in computational aerodynamic predictions [47–50], wind-tunnel testing [7, 9, 19], high incidence angle proprotor aerodynamics [51–53], aero-propulsive modeling [8, 10, 11, 54], flight controls [55, 56], and flight-test strategies [15, 57, 58]. Reference [41] summarizes the research pursuits being undertaken on RAVEN-SWFT.

(a) Front view (cruise configuration)

(b) Overhead view (hover configuration)

(c) Side view (mid-transition configuration)
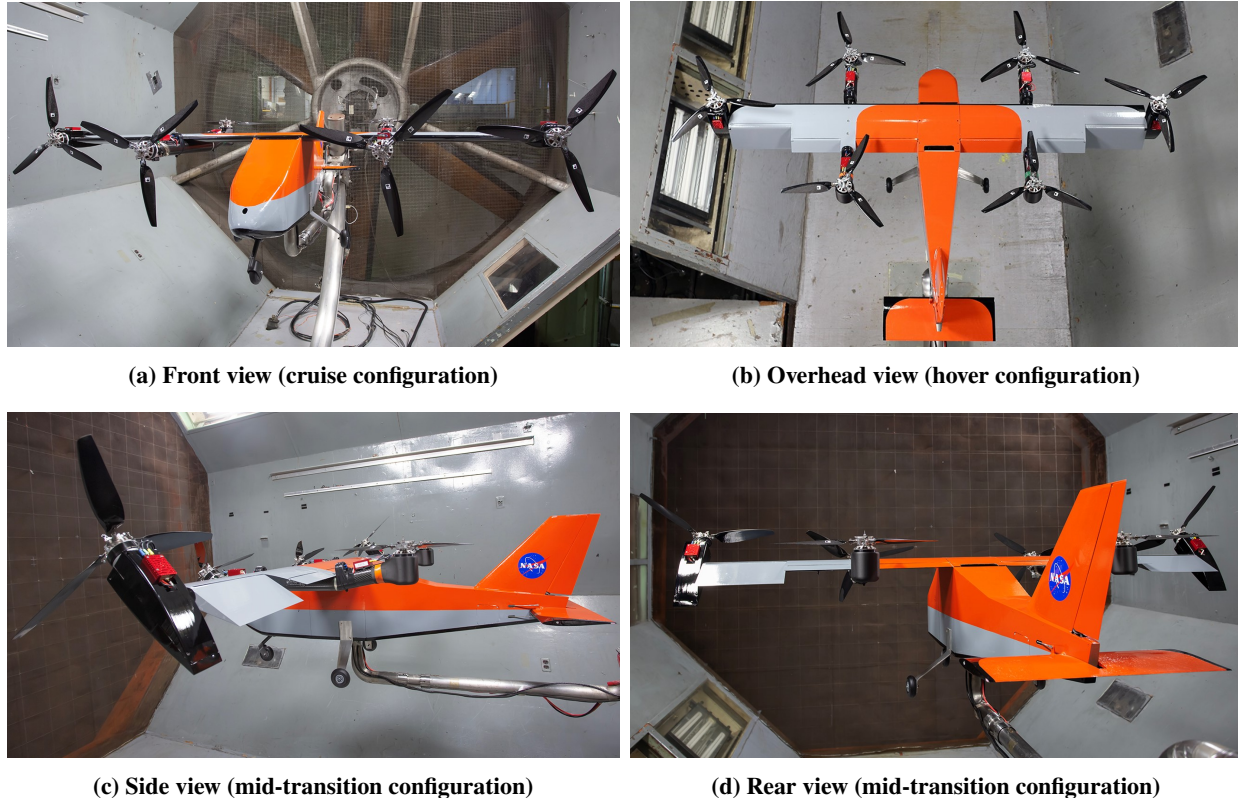
(d) Rear view (mid-transition configuration)

Fig. 2   RAVEN-SWFT mounted in the NASA Langley 12-Foot Low-Speed Tunnel.
(Credit: Lee Pollard, NASA Langley Research Center)

III. Baseline Aero-Propulsive Model

The baseline aero-propulsive model for RAVEN-SWFT was primarily developed using static wind-tunnel tests performed in the NASA LaRC 12-Foot LST for the isolated proprotor [59], the isolated airframe (without proprotors), and powered airframe (with proprotors operating) [12]. Design of experiments (DOE) and response surface methodology (RSM) test techniques [60, 61] were applied throughout the wind-tunnel test campaign [12]. In contrast to traditional one-factor-at-a-time (OFAT) testing, experiments planned using DOE/RSM theory efficiently scale for a large number of test factors, which is essential for characterizing the complex nonlinear aerodynamics and interactions present with eVTOL aircraft. DOE/RSM techniques increase the productivity of data collection by simultaneously varying all test factors in a way that allows efficient determination of the individual contribution of each individual factor, as well as interaction effects among test factors, while fundamentally providing a statistically-rigorous experiment design approach.

The RAVEN-SWFT powered-airframe static wind-tunnel testing and aero-propulsive modeling effort is summarized here to provide context for the present work; additional details are provided in Ref. [12]. The powered-airframe wind-tunnel testing primarily focused on collecting data for flight dynamics simulation development to enable model-based flight control system design. Using test factor ranges reflecting the trimmable transition envelope, static powered-airframe characterization experiments were conducted at eight different dynamic pressure settings from 0 to 5 lbf/ft^2 and independently varied 26 test factors—two airflow orientation angles and the 24 independent control effectors described in Sec. II. A nested I-optimal experiment design approach was used to create the powered-airframe characterization test matrix [12, 54].

RAVEN-SWFT aero-propulsive models were developed from the wind-tunnel data acquired at each tested dynamic pressure setting to produce a transition model for the RAVEN-SWFT vehicle [12]. The form of the model is a set of polynomial response surface equations (RSEs). The modeled responses were the dimensional body-axis aero-propulsive forces X, Y, Z in lbf and moments L, M, N in ft·lbf. The explanatory variables were defined as the body-axis velocity components v, w in ft/s, proprotor rotational speeds $n_1, n_2, \ldots, n_6$ in revolutions per second, proprotor collective pitch angles $\delta_{c_1}, \delta_{c_2}, \ldots, \delta_{c_6}$ in radians, nacelle tilt angles $\delta_{t_1}, \delta_{t_2}, \delta_{t_3}, \delta_{t_4}$ in radians, flaperon deflection angles

$\delta_{f_1}, \delta_{f_2}, \ldots, \delta_{f_6}$ in radians, stabilator deflection angle δ_s in radians, and rudder deflection angle δ_r in radians. Note that forward body-axis velocity u is not included as an explanatory variable, but its effect is implicitly described by the set of aero-propulsive models identified at different dynamic pressure settings. The choice of response variables and explanatory variables follows the eVTOL aircraft modeling convention developed and justified in Ref. [10]. The model structure was determined using stepwise regression and the model parameters were estimated using ordinary least-squares regression [16]. The final aero-propulsive models were shown to have good predictive capability across the tested flight envelope [12]. To form a continuous transition model, the RSEs identified at each dynamic pressure setting were blended using shape-preserving piecewise cubic interpolation [62, 63]. The high-speed transition and forward flight airspeeds for the RAVEN-SWFT vehicle are higher than the airspeed settings that are able to be tested in the 12-Foot LST. Therefore, supplemental computational and/or flight-test model identification efforts are required to produce an aero-propulsive model valid in the high-speed portion of the flight envelope.

The RAVEN-SWFT static wind-tunnel testing yielded a high-fidelity static transition model; however, aerodynamic damping effects are not characterized in static testing and are required to accurately predict aircraft motion in dynamic maneuvering with nonzero angular velocity. The primary goal of the work described in this paper is to identify high-fidelity aero-propulsive damping estimates using 3DOF wind-tunnel testing to supplement the static model and, consequently, improve the accuracy of the RAVEN-SWFT flight dynamics simulation. Prior to conducting the 3DOF wind-tunnel testing used to identify accurate aero-propulsive damping estimates, preliminary damping estimates were still needed for the flight dynamics simulation used to develop a flight control system to stabilize the aircraft on the 3DOF apparatus. The preliminary damping predictions were composed of isolated-airframe damping derivatives computed using FlightStream® [64] and the damping effects manifesting from the difference in relative velocity experienced by each proprotor, similar to the approach described in Ref. [14]. The aerodynamic damping effects associated with propulsion-airframe interactions were not considered for these initial low-fidelity damping estimates, but it is recognized that they have a significant effect. The high-fidelity aero-propulsive damping estimates identified later in the paper do include contributions from interaction effects.

IV. Flight Control System

Electric VTOL aircraft are generally unstable in a significant portion of their flight envelope. Consequently, an active flight control system (FCS) is required to fly the aircraft, perform simulation studies, or conduct the 3DOF free motion wind-tunnel testing that is the subject of this paper. FCS design for complex eVTOL aircraft is challenging for many reasons, including inherent vehicle instability, strong aerodynamic nonlinearities, and aero-propulsive interaction effects. Control allocation strategies are also ambiguous due to the availability of many redundant control effectors that change effectiveness throughout the transition envelope and affect the vehicle response in multiple axes. This section summarizes major aspects of the 3DOF control system development effort for RAVEN-SWFT, including creating a flight dynamics simulation, designing the control system, and integrating the control system onto vehicle hardware.

A. Flight Dynamics Simulation

The flight dynamics simulation was developed in Simulink® and is a modified version of NASA's open source "Flight Dynamics Simulation of a Generic Transport Model" [65], where pertinent changes were made to simulate flight for the RAVEN-SWFT aircraft. The top level of the RAVEN-SWFT simulation Simulink® diagram is shown in Fig. 3, which is composed of the simulation inputs, flight control system, vehicle model, and simulation outputs. The Simulation Inputs subsystem includes simulated radio control (RC) transmitter inputs and ground control station (GCS) commands. The Simulation Outputs subsystem stores, plots, and creates a three dimensional visualization of the simulation data. The Vehicle Model subsystem will be described next and the Flight Control System subsystem will be discussed in Sec. IV.B.

Nonlinear vehicle simulations are performed using the kinematic and dynamic aircraft equations of motion developed under a standard set of assumptions [16, 66, 67]. The aircraft is nominally modeled as a single six degree-of-freedom (6DOF) rigid body subjected to gravitational force and aero-propulsive forces and moments computed using the baseline model discussed in Sec. III. The dynamics associated with the rotating portion of each propulsor and nacelle tilt are neglected in simulations used for control design, since the inertia of rotating components is small compared to that of the vehicle. Because the simulation is used to design a flight controller for a 3DOF wind-tunnel test, in addition to free-flight
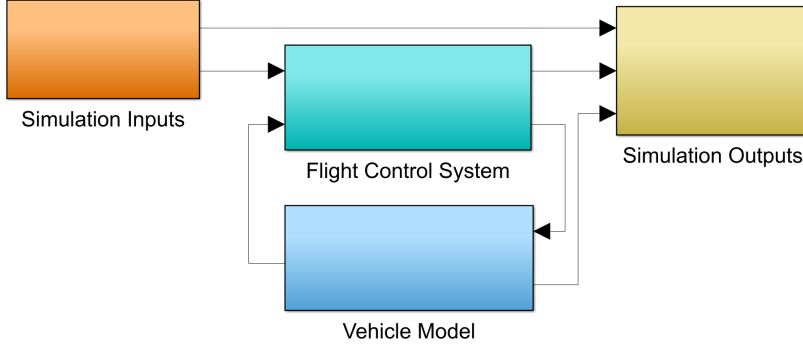
Fig. 3 Top-level view of the RAVEN-SWFT simulation Simulink® diagram.

testing, the 6DOF simulation was programmed to include necessary modifications to conduct 3DOF simulations. For 3DOF simulations, the rotation point is located at the vehicle center of gravity location, which simplifies derivation of the equations of motion. The translational dynamics equations are:

$$\dot{u} = rv - qw + \kappa(-g\sin\theta + X/m) \tag{1}$$

$$\dot{v} = pw - ru + \kappa(g\cos\theta\sin\phi + Y/m) \tag{2}$$

$$\dot{w} = qu - pv + \kappa(g\cos\theta\cos\phi + Z/m) \tag{3}$$

The κ parameter is used to switch between 3DOF and 6DOF simulations, where $\kappa = 0$ for 3DOF simulations and $\kappa = 1$ for 6DOF simulations. The rotational dynamics equations are:

$$I_x\dot{p} - I_{xz}\dot{r} = L + (I_y - I_z)qr + I_{xz}pq \tag{4}$$

$$I_y\dot{q} = M + (I_z - I_x)pr + I_{xz}(r^2 - p^2) \tag{5}$$

$$I_z\dot{r} - I_{xz}\dot{p} = N + (I_x - I_y)pq - I_{xz}qr \tag{6}$$

The rotational dynamics equations are the same for 3DOF and 6DOF simulations. The simulation also included models for motor performance, control surface servo-actuator dynamics, motor dynamics, ground contact, sensors, wind, and atmospheric turbulence.

B. Flight Control System Design

The flight control algorithm was developed with a model-based design approach, using the RAVEN-SWFT flight dynamics simulation. The model-based approach allows for specification of performance and robustness requirements, use of optimal control techniques for gain tuning, rapid development in a simulation environment, and increased confidence in the flight control solutions for vehicle testing [68].

The overall RAVEN-SWFT flight control algorithm is composed of a nested-loop architecture, depicted in Fig. 4, including an attitude-control inner loop and a velocity-control outer loop. The design approach includes a robust servomechanism linear quadratic regulator [69] control framework with a feedforward element. The nested-loop structure enables sequential design of the control system, from inner to outer loops, as well as multiple entry points for piloted testing. The inner- and outer-loop control laws have a similar internal structure, shown in Fig. 5. Each has filtered sensor data used for feedback stabilization and reference tracking, a feedforward path for transient response shaping, and a control allocation scheme to appropriately distribute the control system commands. The flight control law feedback gains, trim settings, control allocation, and other FCS parameters are scheduled with dynamic pressure to create a full-envelope flight controller that transitions the aircraft from hover to forward flight. For 3DOF wind-tunnel testing, only the inner-loop control laws are active and track reference roll, pitch, and yaw attitude commands, while automatically transitioning the aircraft based on the freestream dynamic pressure. The inner-loop control laws output force and moment commands, which are distributed to the various control effectors using a weighted pseudo-inverse control allocation strategy.
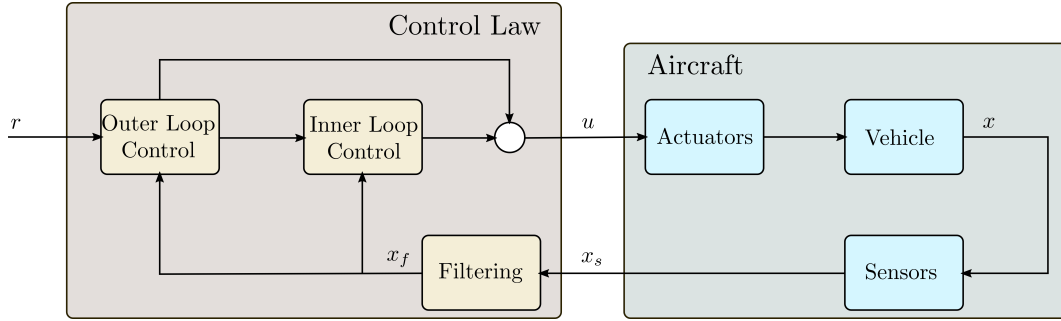
Fig. 4 Schematic of the overall RAVEN-SWFT flight control algorithm.
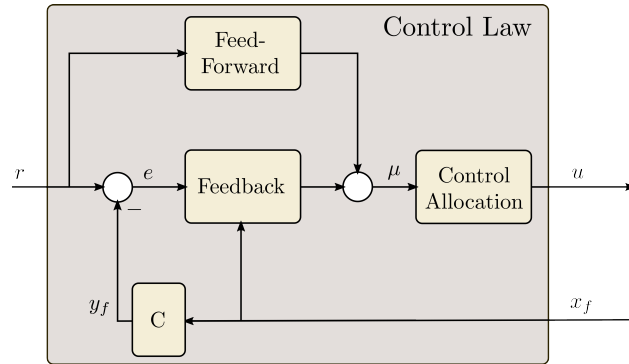

Fig. 5 Schematic of the inner- and outer-loop control law structure.

The design of the flight control algorithm is based on linearization of the nonlinear flight dynamics simulation at trim conditions. Trim settings, where the sum of gravitational and aero-propulsive forces and moments are equal to zero, were determined across the flight envelope using the constraining nonlinear optimization function `fmincon` available in MATLAB® [70]. The optimization objective function was the total motor power usage added to the sum of each motor rotational speed and collective pitch angle in coded units, formed from the operational bounds, raised to an even power. The objective function balances minimizing power consumption (i.e., maximizing vehicle range) and maximizing the available propulsion control authority. Figure 6 provides a visualization of the scheduled nacelle tilt angle trim settings used for 3DOF wind-tunnel testing. As mentioned previously, the high-speed transition and forward flight airspeeds for the RAVEN-SWFT vehicle are higher than are able to be tested in the 12-Foot LST, which is why the full transition envelope is not shown in this figure.
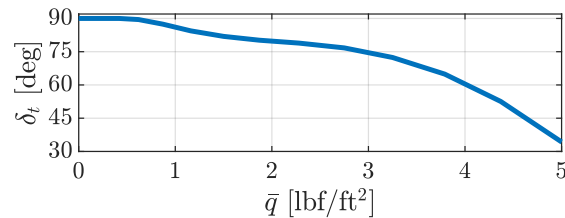

Fig. 6 Variation of RAVEN-SWFT nacelle tilt angle (δ_t) trim settings with dynamic pressure.

Control performance and robustness analyses were performed using both the linearized and nonlinear flight dynamics model. Control synthesis accounted for closed-loop robustness, actuator usage, measurement noise propagation, and gain and time-delay margin predictions.

C. Flight Control System Integration

In parallel to simulation-based RAVEN-SWFT FCS development, efforts were undertaken to identify a streamlined solution to deploy a custom Simulink® model onto flight vehicle hardware. Through the use of low-cost surrogate vehicles, a process to deploy custom flight control logic developed in Simulink® onto a Pixhawk flight computer was identified and refined [71, 72]. The flight controller deployment process, which uses the MathWorks® UAV Toolbox and its Support Package for PX4 Autopilots [70], was determined to be a suitable solution for RAVEN-SWFT with a few vehicle hardware related modifications. The control algorithm replaces the default PX4 outer- and inner-loop control logic with custom control laws but retains most of the other functionality in the PX4 Autopilot firmware, such as the state estimation algorithm, input/output drivers, safety logic, and data logging capabilities. These methods allow for rapid deployment of a custom flight controller, where a new control software update can be built and deployed onto the Pixhawk flight computer in under five minutes.

After the RAVEN-SWFT FCS was designed and tested in simulation, steps were taken to integrate the control logic onto the vehicle hardware. Initially, simulations were executed with the Simulink® model running on a laptop computer and communicating with the vehicle sensors, control effectors, and RC transmitter/receiver. Then, the Simulink® model was autocoded onto a Pixhawk flight computer to execute experimental testing. The top level of the flight control software Simulink® diagram used for integration onto the RAVEN-SWFT vehicle is shown in Fig. 7. The overall structure is similar to the simulation structure shown in Fig. 3, except that the FCS Input and FCS Output subsystems in Fig. 7 are used to interface with the vehicle and the vehicle model is replaced by the actual vehicle dynamics. The FCS Inputs subsystem includes functionality to read RC transmitter inputs, sensor data, PX4 state estimates, and GCS commands. The FCS Outputs subsystem sends commands to the control effectors, transmits data to the GCS, and logs internal flight control signals. The Flight Control System subsystem is identical to the equivalent subsystem shown in Fig. 3; the subsystem contains the control laws described in Sec. IV.B, as well as other logic necessary to safely fly the vehicle and the programmed test input (PTI) injection capabilities discussed next.

FCS Inputs   Flight Control System   FCS Outputs

Fig. 7   Top-level view of the flight control software Simulink® diagram integrated onto the vehicle.

V. Experiment Design

A system identification experiment must be properly executed to generate informative data that can be used to identify an accurate model. The RAVEN-SWFT FCS is configured to inject PTI excitations before and after the flight control laws, as shown in Fig. 8. To execute a system identification maneuver, PTI excitations are injected into the reference attitude commands and control effector commands, while the flight controller simultaneously stabilizes the vehicle and tracks the commanded attitude.
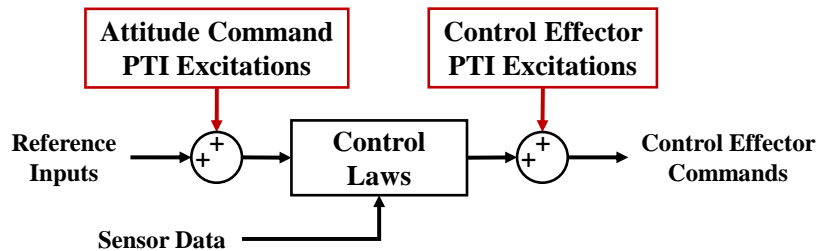

Fig. 8   Programmed test input injections relative to the control laws.

Orthogonal phase-optimized multisine inputs, described in further detail in Refs. [16, 73–75], are the primary PTI type used for this work. A multisine input is defined as a sum of multiple sinusoidal functions with different amplitudes,

frequencies, and phase angles, where the frequencies are chosen to encompass the frequency range corresponding to the system dynamics of interest. To make all inputs orthogonal in both the time domain and frequency domain, the multisine signal for the jth control effector is assigned sinusoids with a unique subset K_j of discrete harmonic frequency indices selected from the complete set of K available frequency indices. The available frequencies in Hz are $f_k = k/T, \; k = 1, 2, ..., K$, where T is the fundamental period and K/T is the highest excitation frequency. For m total control effectors, the jth input signal $\boldsymbol{u}_j$ is defined as

$$\boldsymbol{u}_j = \sum_{k \in K_j} A_j \sqrt{P_k} \sin\left(\frac{2\pi k \boldsymbol{t}}{T} + \phi_k\right), \quad j = 1, 2, ..., m \tag{7}$$

where A_j is the signal amplitude, P_k is the kth power fraction (with $\sum_{k \in K_j} P_k = 1$), ϕ_k is the kth phase angle defined on the interval $(-\pi, +\pi]$, and $\boldsymbol{t}$ is the time vector containing N discrete points. The relative peak factor

$$\text{RPF}\,(\boldsymbol{u}_j) = \frac{1}{\sqrt{2}} \frac{\left[\max\,(\boldsymbol{u}_j) - \min\,(\boldsymbol{u}_j)\right] / 2}{\sqrt{\boldsymbol{u}_j^T \boldsymbol{u}_j / N}} \tag{8}$$

is the range of input amplitude divided by the root-mean-square of the signal, referenced to the peak factor for a single frequency sinusoidal signal. The multisine signal phase angles are optimized to obtain a minimum RPF, which helps to keep the system close to its nominal operating point while retaining the same input energy as a signal composed of the same amplitude and frequency sinusoidal functions without optimized phase angles. Minimizing the RPF also keeps the control effector rates of change low, which is beneficial for repetitive dynamic use of the electric motors and control surface servo-actuators during testing. Because all control effectors and aircraft dynamics of interest can be simultaneously excited, the use of multisine inputs facilitates execution of highly efficient and informative testing. A single multisine maneuver can be used to develop a comprehensive aircraft dynamic model around a nominal flight condition, including nonlinear aerodynamic phenomena and control interaction effects.

For RAVEN-SWFT 3DOF wind-tunnel testing, individual multisine signals were generated for each of the 24 independent control effectors. Additionally, multisine signals were created for the roll, pitch, and yaw angle commands tracked by the control system to provide additional state perturbations supplementing state disturbances resulting from control effector PTI injections. The multisine yaw angle commands were noted to be particularly useful for improving the parameter estimate values associated with lateral speed v and yaw rate r. Combining the control effector and attitude command multisine signals, which are all executed simultaneously, there are a total of 27 independent excitation signals.

Several harmonic components were assigned to each multisine signal, where the overall frequency range was set to between 0.05 Hz and 1.75 Hz in accordance with frequencies where the rigid-body dynamics were expected to manifest. The harmonic components for the attitude commands and slower moving control effectors were selected in accordance with the approximate bandwidth of each signal. The collective pitch, outboard tilt, stabilator, flaperon, and rudder multisine signal harmonic components spanned the full frequency range and were each assigned 18 frequency components. The proprotor rotational speed, inboard tilt, and attitude command harmonic components were focused into lower frequencies due to their lower bandwidth and contained 16, 12, and 5 frequency components, respectively. The frequency components were assigned to each signal in an alternating manner and were distributed to avoid neighboring control effectors having neighboring frequency components, similar to the approach described in Ref. [76].

The input spectra for the final set of orthogonal phase-optimized multisine signals is shown in Fig. 9. There are 423 total harmonic components with a fundamental period of $T = 260$ seconds. The overall frequency range is between $f_{\min} = 0.05$ Hz and $f_{\max} = 1.735$ Hz with a frequency resolution of $\Delta f = 1/T = 0.00385$ Hz. Figure 10 shows the first 20 seconds of the input excitation signals with an amplitude A_j of one. For system identification experiments, a gain is applied to scale each input signal to a sufficient amplitude to obtain a good signal-to-noise ratio, while not deviating far from the trimmed flight condition. The maneuver length used for system identification is different than the 20-second input signal duration shown for demonstration purposes in Fig. 10.

Because eVTOL aircraft dynamics are generally unstable over a large portion of the transition flight envelope, a feedback control system must be active when operating the aircraft. Although necessary for safety, flight control systems can create deficiencies in the data information content available for system identification. Control systems act to suppress the natural aircraft motions that system identification maneuvers are designed to excite, distort optimally designed control inputs, and lead to correlation between explanatory variables, making their independent effects more difficult to distinguish. Fortunately, when multisine signals are summed with the control effector commands downstream of the control system, as shown in Fig. 8, the adverse effects of the flight control system on the system identification experiment
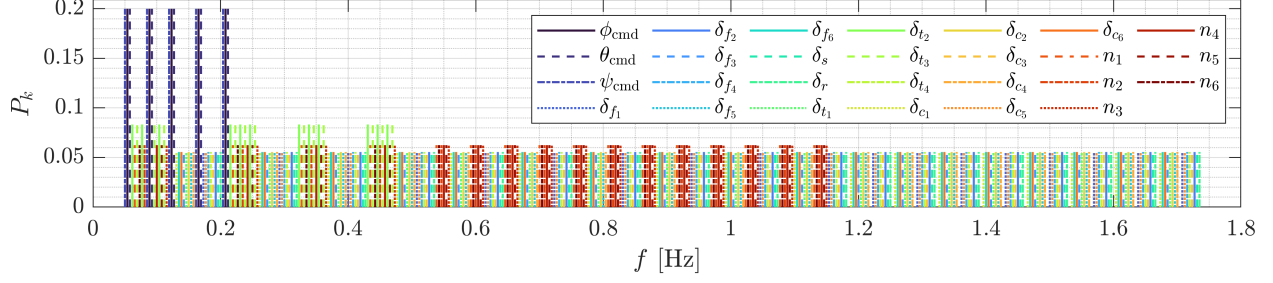
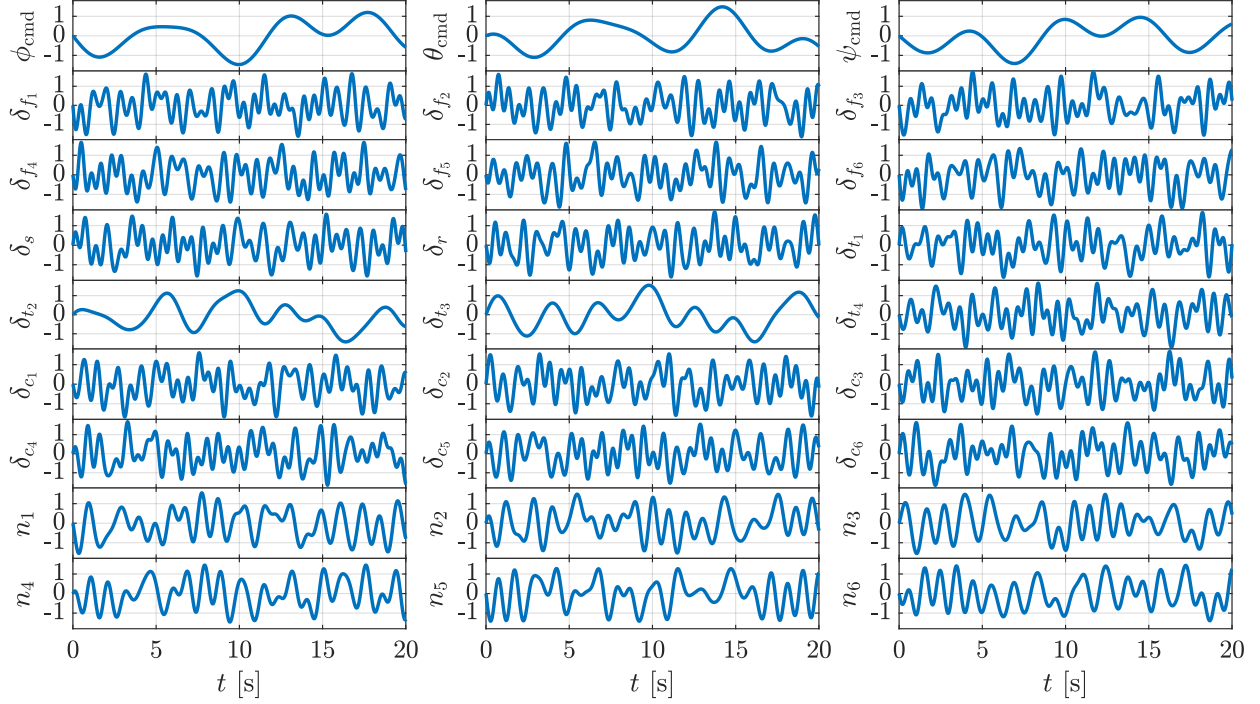**Fig. 9 Multisine input spectra for each attitude command and control effector.**

Fig. 10 Normalized multisine input signal for each attitude command and control effector.

are mitigated. The control signals sent to the motors and actuators will differ from the designed multisine waveforms due to actions from the FCS, but even with this distortion, the modeling variables are still sufficiently decorrelated for model identification as a result of injecting the excitation inputs after the flight control laws [16, 75].

In addition to multisine inputs, the RAVEN-SWFT FCS was programmed to be able to inject multistep square wave inputs (e.g., doublet, 1-2-1, and 3-2-1-1 inputs) and frequency sweep inputs as attitude command PTIs. Doublet (1-1) commands were used to assess control system attitude tracking performance prior to conducting system identification experiments. Frequency sweep and the more complex multistep inputs were not used for the work described in this paper. Due to the large number of control effectors and aero-propulsive complexity associated with eVTOL vehicles, multisine inputs are the preferred input type for efficient open-loop model identification.

VI. Wind-Tunnel Testing
The RAVEN-SWFT free motion wind-tunnel testing was conducted at the NASA LaRC 12-Foot LST [43]. The 3DOF apparatus, instrumentation, and test execution strategy are described in the remainder of this section.

A. Three Degree-of-Freedom Apparatus

A new 3DOF free motion test rig was recently designed and built by the Flight Dynamics Branch at NASA LaRC. The RAVEN-SWFT vehicle mounted on the 3DOF apparatus in the 12-Foot LST is shown in Fig. 11. The 3DOF rig allows for free simultaneous roll, pitch, and yaw motion. Any of the rotation axes can be fixed for 1DOF or 2DOF testing. The 3DOF rig was robustly designed to accommodate the loading requirements for a variety of vehicles able to be tested in the 12-Foot LST, as well as the new Flight Dynamics Research Facility (FDRF) currently being built at NASA LaRC [77]. Applying the approach discussed herein, the 3DOF rig allows for rapid extraction of aerodynamic damping derivatives in a way that is faster than traditional forced oscillation testing. Furthermore, the 3DOF rig allows for flight control logic to be efficiently tested in a low-risk environment. Based on the observed performance and data from 3DOF wind-tunnel testing, adjustments to flight control software can be rapidly implemented and verified prior to subjecting a vehicle to the risks of flight testing.

Fig. 11   RAVEN-SWFT vehicle mounted on a 3DOF free motion wind-tunnel apparatus.
(Credit: Lee Pollard, NASA Langley Research Center)

B. Instrumentation

The 3DOF wind-tunnel test instrumentation included sensors onboard the vehicle, embedded in the 3DOF apparatus, and pre-existing in the wind-tunnel system. For 3DOF free motion experiments, the desired measurements are Euler orientation angles, body-axis angular rates, air data parameters, control surface deflection angles, and propulsor rotational speeds. Installation of a force measurement device between the vehicle and 3DOF rig would be a useful addition for future testing, but was not implemented for this work.

Sensors installed with the Pixhawk include rate gyros and an airspeed sensor. The PX4 state estimation algorithm provides bias-corrected filtered angular velocities, quaternion estimates, and air data estimates. These sensor and state estimate data were logged on the Pixhawk, along with the control effectors commands sent by the FCS and other internal FCS signals. (Additional sensors and state estimates are available on the Pixhawk that are crucial for flight testing, but are less important for 3DOF wind-tunnel testing.) Furthermore, the signals from rotary encoders embedded in the 3DOF rig were sent to the Pixhawk to provide a direct source of orientation angles that were recorded and available to the control algorithm. Significant electromagnetic interference effects caused by operating in the wind-tunnel environment, including the close proximity to the wind-tunnel fan motor, were noted to corrupt the PX4 attitude state estimates; consequently, using the rotary encoder angles as the attitude solution was found to be more reliable for real-time feedback control and post-test data analysis. In addition to the signals logged on the Pixhawk, a vehicle data acquisition system also recorded the control commands received by the control surface servo-actuators and motor electronic speed controllers (ESCs), as well as position feedback from the servo-actuators and motor rotational speed from the ESCs. Finally, the wind-tunnel dynamic pressure measurement was used to set the desired test condition.

The body-axis translational velocity components and airflow angles are not directly measured and must be calculated from other measurements. The body-axis velocity components are calculated from the measured freestream velocity

and Euler orientation angles as:

$$u = V \cos \theta \cos \psi \tag{9}$$

$$v = V(\cos \psi \sin \theta \sin \phi - \cos \phi \sin \psi) \tag{10}$$

$$w = V(\cos \psi \sin \theta \cos \phi + \sin \phi \sin \psi) \tag{11}$$

The airflow angles are then computed using:

$$\alpha = \tan^{-1}(w/u) \tag{12}$$

$$\beta = \sin^{-1}(v/V) \tag{13}$$

C. Test Execution

A 3DOF wind-tunnel run was initiated by adjusting the tunnel dynamic pressure to a desired setting while the vehicle was resting on the 3DOF rig attitude stops with the FCS disabled. Then, once the wind-tunnel dynamic pressure stabilized, the FCS was enabled at the test condition and began tracking the commanded vehicle attitude. Apart from setting the dynamic pressure, the 3DOF test was conducted using an RC transmitter and a GCS computer to remotely communicate with the vehicle. The RC transmitter was used to execute the FCS startup sequence, command attitude perturbations from the trim condition, and switch between various FCS and PTI modes. The GCS computer was used to adjust numerous FCS and PTI parameters.

The RAVEN-SWFT 3DOF wind-tunnel testing began by evaluating the FCS performance throughout the test envelope. Piloted doublet and automated square wave PTI inputs were commanded in each axis to assess the controller tracking performance. Although the initial design of the model-based controller performed adequately at most test conditions, certain conditions required feedback gain adjustments to achieve the desired performance. These initial FCS performance deficiencies were primarily attributed to inaccuracies in the low-fidelity aerodynamic damping estimates described in Sec. III, which were updated after completing the 3DOF wind-tunnel test campaign using the results from this paper. Flight control gain adjustments to address the observed deficiencies were able to be made on the GCS computer and sent to the vehicle in real time as required to achieve the desired FCS performance.

After the desired controller performance was achieved across the transition envelope, the focus of the test shifted to acquiring system identification data for aero-propulsive damping characterization. Starting from a trimmed flight condition, a multisine maneuver was enabled by a switch on the RC transmitter. The vehicle FCS then injected multisine signals into the control effector and attitude commands, perturbing the vehicle around its reference conditions without requiring any additional pilot or GCS inputs. Multisine maneuvers were disabled after approximately 60 seconds had elapsed using an RC transmitter switch, and the vehicle subsequently returned to the trimmed flight condition. To achieve an appropriate amount of vehicle excitation, the overall PTI amplitude could be scaled in real time using a rotary knob on the RC transmitter. Furthermore, the multisine amplitude could be separately scaled for each group of control effectors (e.g., outboard flaperons, inboard flaperons, front collective, rear collective, etc.) and each attitude command. Other PTI types could also be executed and adjusted using similar procedures.

System identification data were collected at the seven nonzero dynamic pressure settings used to develop the static RAVEN-SWFT aero-propulsive model [12]:

$$\bar{q} = [0.25 \quad 0.62 \quad 1.16 \quad 1.87 \quad 2.75 \quad 3.79 \quad 5.00] \text{ lbf/ft}^2$$

At standard sea level conditions, the corresponding freestream velocity settings, which vary linearly between the lowest and highest practical settings for testing in the 12-Foot LST, are:

$$V = [14.5 \quad 22.9 \quad 31.3 \quad 39.7 \quad 48.1 \quad 56.5 \quad 64.9] \text{ ft/s}$$

At each freestream condition, at least five 60-second multisine maneuvers were executed for identification of the dynamic aero-propulsive model. Note that, however, the data acquired during a single 60-second multisine maneuver are adequate for model development. Replicate maneuvers were collected in this study to investigate repeatability and improve parameter estimation accuracy, but are not required to develop an accurate model.

VII. Modeling Approach

The modeling approach applied to 3DOF wind-tunnel experiments is similar to the strategy used to create a static aero-propulsive model from wind-tunnel testing (see Sec. III). Separate dynamic aero-propulsive models are developed at each dynamic pressure setting to produce a transition model for the RAVEN-SWFT vehicle. The modeled responses are the dimensional body-axis moments L, M, N in ft·lbf. The vehicle was not instrumented to measure the applied aero-propulsive forces X, Y, Z while operating on the 3DOF rig, so these responses are not modeled. As will be discussed later in Sec. IX, this omission is considered to be a minor nuisance for the present application. The explanatory variables are the same as those stated in Sec. III, except that body-axis angular velocity components p, q, r in rad/s are also included to capture aero-propulsive damping effects.

Although the applied aero-propulsive moments are defined as the responses to be modeled, these quantities are not measured directly on the 3DOF apparatus and must be inferred from other measurements. The applied moments are calculated using the rotational dynamic equations [cf. Eqs. (4)-(6)] as:

$$L = I_x \dot{p} - I_{xz} \dot{r} + (I_z - I_y)qr - I_{xz}pq \tag{14}$$

$$M = I_y \dot{q} + (I_x - I_z)pr + I_{xz}(p^2 - r^2) \tag{15}$$

$$N = I_z \dot{r} - I_{xz} \dot{p} + (I_y - I_x)pq + I_{xz}qr \tag{16}$$

The body-axis angular accelerations $\dot{p}, \dot{q}, \dot{r}$ within Eqs. (14)-(16) are calculated using smoothed numerical differentiation of the body-axis angular rates [16, 78]. The transient torque and gyroscopic effects from the propulsors and tilt nacelles are assumed to be small relative to the applied moments and are thus neglected.

Parameter estimation was performed using the equation-error method formulated in the frequency domain [16, 78, 79]. The benefits of this method include least-squares weighting based on frequency components, accurate parameter uncertainty estimates, and computational efficiency. To implement the frequency-domain modeling approach, the regressor and response variable data are first detrended; then, the data are transformed into the frequency domain using a high-accuracy Fourier transform technique that leverages time-domain cubic interpolation and the chirp-z transform, which allows for specification of an arbitrary frequency range and resolution [16, 80]. Here, the Fourier transform frequencies are set between $f_{\min} = 0.05$ Hz and $f_{\max} = 1.8$ Hz with a frequency resolution of $\Delta f = 0.001$ Hz. An additional benefit is realized by performing modeling using a restricted frequency range, which effectively smooths the data and allows for estimation of nearly unbiased parameter estimates when the regressors contain noise [16, 78, 79].

Parameter values are estimated using ordinary least-squares regression with the complex regressor and response data. Ordinary least-squares regression is used to estimate the p unknown model parameters in a parameter vector θ for a given model $\tilde{y} = \tilde{X}\theta$, where $\tilde{y}$ is the length M complex model response vector and $\tilde{X}$ is a $M \times p$ matrix consisting of column vectors of the complex regressors assumed to be error-free [16]. The measurement equation is

$$\tilde{z} = \tilde{X}\theta + \tilde{v} \tag{17}$$

where $\tilde{z}$ is the complex measured response variable corrupted by constant variance, zero-mean, and uncorrelated complex error $\tilde{v}$. For complex least-squares parameter estimation, the optimal estimate of the unknown parameters is obtained by minimizing the cost function:

$$J(\theta) = \frac{1}{2} \left(\tilde{z} - \tilde{X}\theta \right)^{\dagger} \left(\tilde{z} - \tilde{X}\theta \right) \tag{18}$$

The optimal estimate of the unknown real-valued parameters is then determined as

$$\hat{\theta} = \left[Re \left(\tilde{X}^{\dagger} \tilde{X} \right) \right]^{-1} Re \left(\tilde{X}^{\dagger} \tilde{z} \right) \tag{19}$$

and modeled response variable vector is:

$$\hat{\tilde{y}} = \tilde{X}\hat{\theta} \tag{20}$$

A length p vector of standard errors $s(\hat{\theta})$ corresponding to the estimated parameters $\hat{\theta}$ is given as:

$$s(\hat{\theta}) = \sqrt{\left(\frac{1}{2T\left(f_{\max} - f_{\min}\right)} Re \left[\left(\tilde{z} - \hat{\tilde{y}} \right)^{\dagger} \left(\tilde{z} - \hat{\tilde{y}} \right) \right] \right) \ \text{diag} \left(\left[Re \left(\tilde{X}^{\dagger} \tilde{X} \right) \right]^{-1} \right)} \tag{21}$$

13

This form of $s(\hat{\theta})$ accounts for the fact that an arbitrary frequency range is used for analysis [79].

The model parameters computed using complex least-squares parameter estimation only capture dynamic information, therefore, an additional step is required to determine the bias term in a model equation [16, 79]. The scalar bias parameter estimate $\hat{\theta}_o$ is found as the mean value of $(z - X\hat{\theta})$, where z is the measured response variable in the time domain, X is a matrix consisting of column vectors of the regressors in the time domain, and $\hat{\theta}$ is the model parameter vector estimated previously using complex least-squares regression in Eq. (19). The standard errors for the bias parameters were estimated accounting for colored residuals using the method described in Refs. [16, 81] to compute a more accurate estimate of parameter uncertainty.

Least-squares regression estimates the values of model parameters in a fixed model structure. Consequently, a method of determining an adequate model structure is required. The model structure for each response variable at each dynamic pressure setting was determined using stepwise regression procedures [16, 82, 83]. To implement the stepwise regression technique, a set of candidate model terms is postulated as polynomial expansions of the explanatory variables, including nonlinear and cross terms. The candidate terms are then added or removed from the model to assess the significance of including each model term. Linear terms in the polynomial model structure are incorporated first, followed by nonlinear terms. For this effort, in general, the model structure for each response variable was mostly linear with an occasional nonlinear state variable term. Although parameters were estimated for all state and control variables, the terms of primary interest are those involving the angular rates p, q, r to characterize the aero-propulsive damping effects (i.e., the model terms that were not included in the previously developed static aero-propulsive model). The damping model parameters determined to be significant were L_p, L_r, M_q, N_p, and N_r; these model parameters were included in the model structure at each flight condition.

The final parameter estimates at a reference flight condition were calculated by combining the parameter estimation results obtained for a set of n independent maneuvers collected at the particular flight condition. The most probable final estimate of a scalar parameter is formed by the weighted mean [84]:

$$\hat{\theta} = \frac{\sum_{i=1}^{n} \left[\hat{\theta}_i / s_i^2 \right]}{\sum_{i=1}^{n} \left[1/s_i^2 \right]} \tag{22}$$

Here, $\hat{\theta}_i$ and s_i are the parameter estimate and standard error values, respectively, computed for an individual parameter from the ith maneuver. The corresponding scalar propagated uncertainty estimate σ for the final parameter estimate $\hat{\theta}$ is [84]:

$$\sigma = \sqrt{\frac{1}{\sum_{i=1}^{n} \left[1/s_i^2 \right]}} \tag{23}$$

VIII. Results

As outlined previously, the modeling approach used for this effort was to identify aero-propulsive models throughout the RAVEN-SWFT test envelope around a set of predetermined trimmed reference conditions. The primary results desired from 3DOF experiments were dynamic derivative estimates to supplement the previously identified static model. To demonstrate the approach, sample local modeling results from a reference flight condition are provided followed by a summary of global modeling results.

A. Local Modeling Results

Data collected during a sample multisine maneuver at a reference dynamic pressure of 2.75 lbf/ft^2 is plotted in Fig. 12. The control signals shown in Fig. 12 are different from the designed signals shown in Fig. 10 due to distortion from the FCS, but are still sufficiently decorrelated for model identification as a result of the implementation approach discussed in Sec. V. For each maneuver, the last 10 seconds of data were withheld from the modeling process and used for model validation; the remaining approximately 50 seconds of data from the first part of the maneuver were used for model identification. Although it is generally considered a best practice to use a validation input signal that differs from the waveform used for modeling, for eVTOL aircraft, it is challenging to execute an efficient and rigorous prediction test due to the large number of control effectors. This is why a multisine maneuver was used for both model identification and validation. The modeling and validation data are from different parts of the designed multisine maneuver, so the validation data character is still different from the portion of the maneuver used for model identification.

The frequency-domain model fits to the aero-propulsive moment components for the maneuver shown in Fig. 12 are displayed in Fig. 13. An excellent model fit is observed for each response variable. The frequency-domain coefficient of
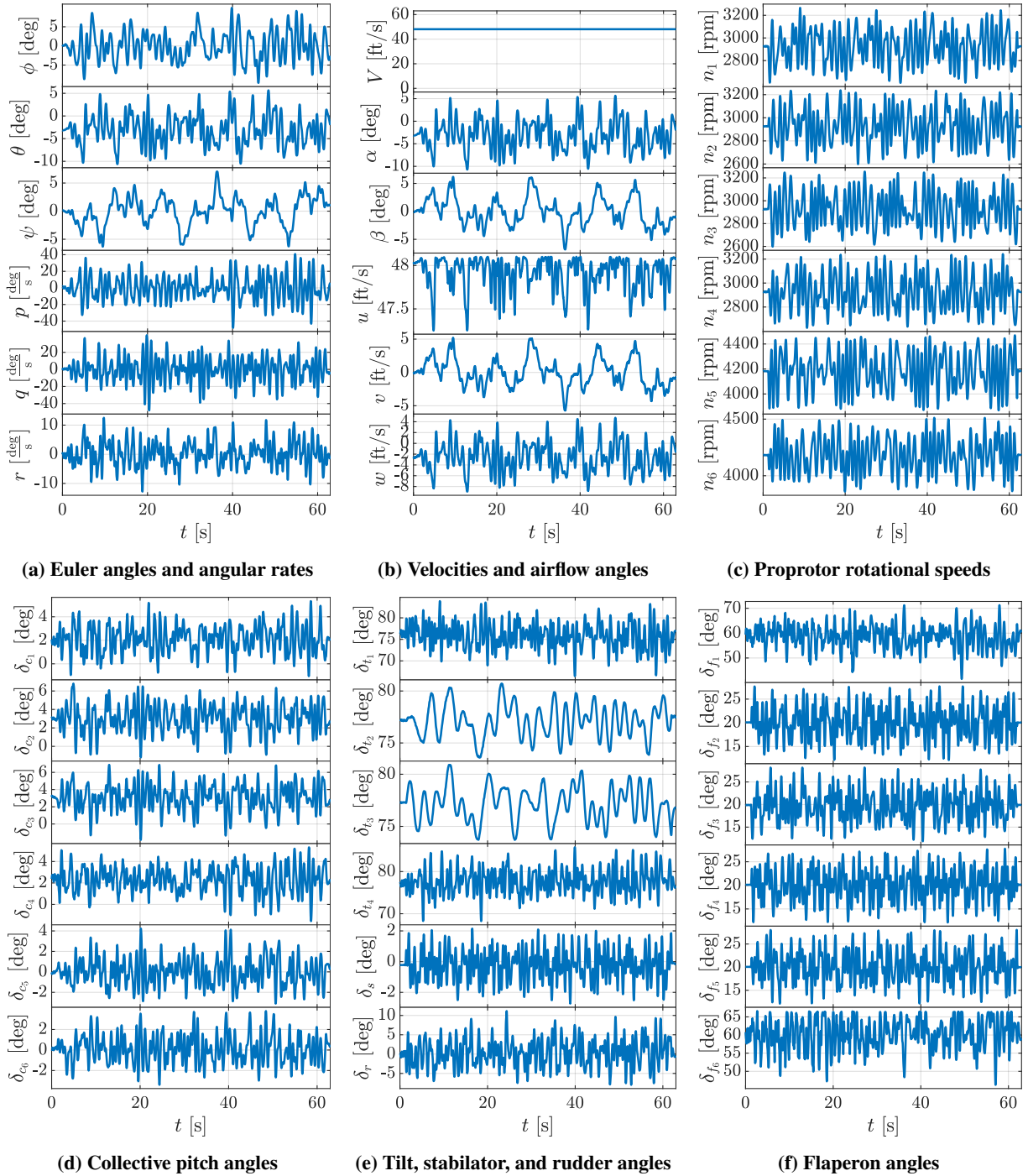
(a) Euler angles and angular rates

(b) Velocities and airflow angles

(c) Proprotor rotational speeds

(d) Collective pitch angles

(e) Tilt, stabilator, and rudder angles

(f) Flaperon angles

Fig. 12 Example data from a multisine maneuver at $\bar{q}$ = 2.75 lbf/ft^2.

determination, R^2, shown on the plot for each response is high, indicating that most of the variation of the response variable about its mean is characterized by the model. Similar model fit results were obtained for other multisine maneuvers executed at this flight condition.

After the parameter estimates for each individual maneuver at the reference condition were identified, the final weight-mean parameter estimate and uncertainty values were determined using Eqs. (22)-(23). Figure 14 shows the time-domain model predictions compared to the smoothed aero-propulsive moment data calculated from the data shown
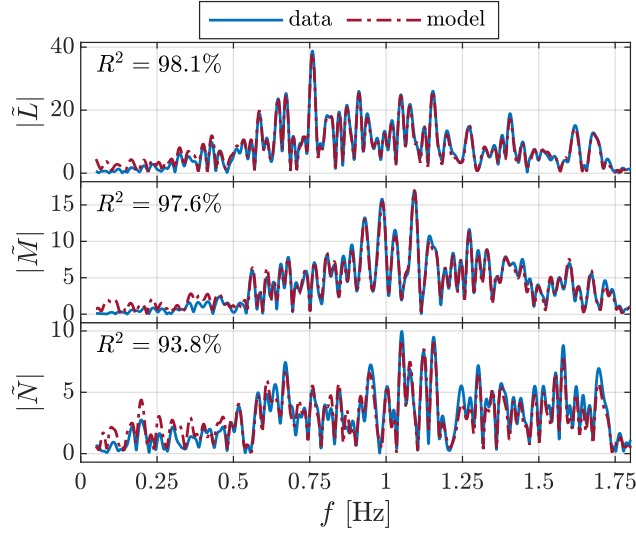
Fig. 13   Comparison of modeling response data and model fit in the frequency domain for a multisine maneuver at $\bar{q}$ = 2.75 lbf/ft^2.

in Fig. 12. The model prediction closely follow the data used for modeling, as well as the validation data, suggesting that model is able to characterize a large amount of the variation in each response. The local model prediction capability was similar for other maneuvers at this reference condition.
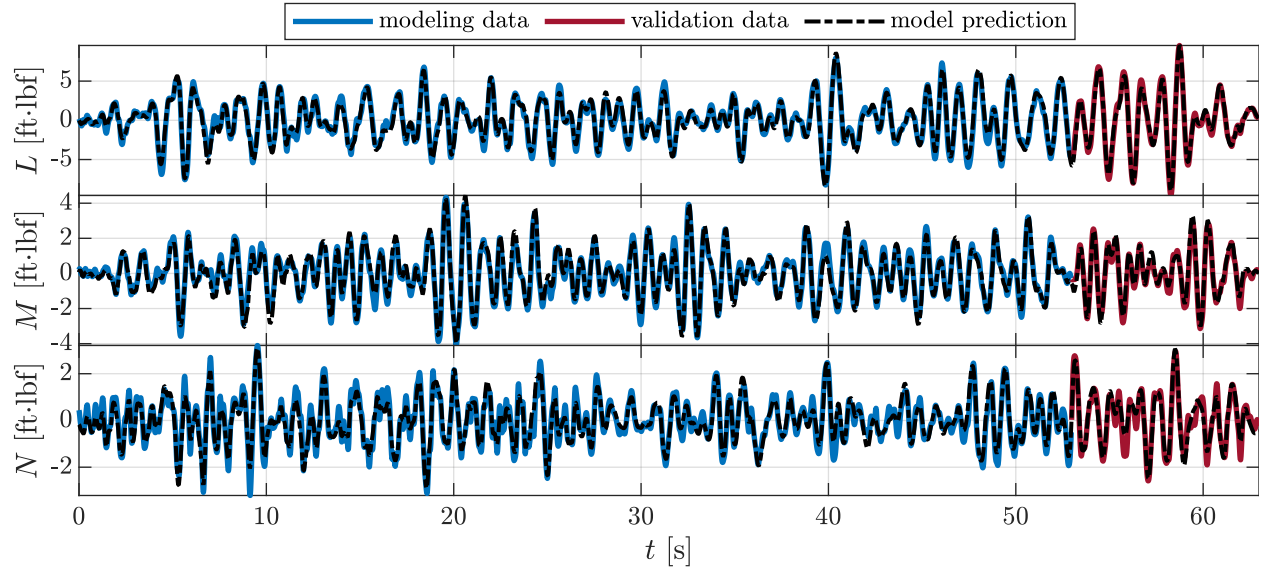

Fig. 14   Comparison of time-domain response data and model prediction for a multisine maneuver at $\bar{q}$ = 2.75 lbf/ft^2.

B. Global Modeling Results

Execution of similar multisine maneuvers occurred across the RAVEN-SWFT flight envelope and was followed by the same local modeling procedures. The average frequency domain R^2 values at each flight condition are displayed in Fig. 15. Most local models have an R^2 value near or above 90%, indicating that a significant portion of the variation in the response is described by the models. The R^2 values for pitching moment M are observed to be lower at $\bar{q}$ = 1.16 lbf/ft^2 and $\bar{q}$ = 1.87 lbf/ft^2, which corresponds to a challenging pitch control condition in the RAVEN-SWFT

transition envelope. Nonetheless, the R^2 values are adequate for each response at all test conditions.
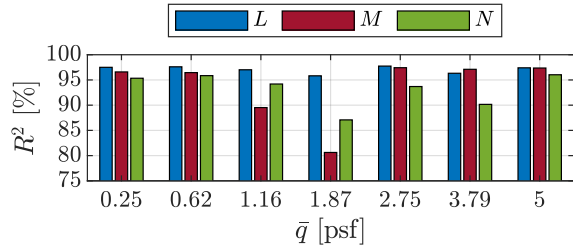

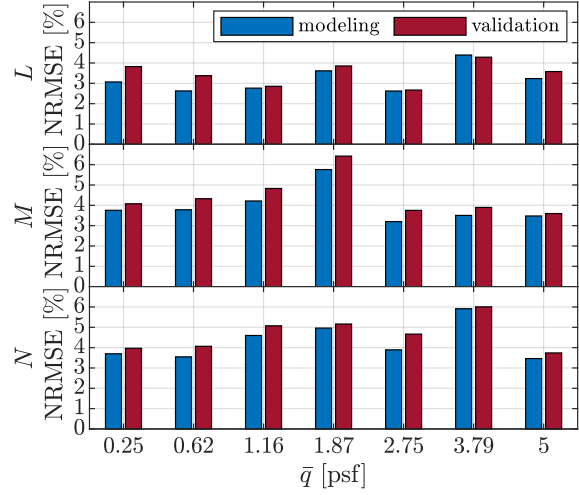**Fig. 15 Average coefficient of determination, R^2, at each reference dynamic pressure.**

Fig. 16 Modeling and validation NRMSE at each reference dynamic pressure.

The response prediction capability for the modeling and validation data acquired using multisine maneuvers can be quantified and compared using the normalized root-mean-square error (NRMSE) metric, expressed as a percentage, as

$$\text{NRMSE} = 100 \times \frac{1}{\text{range}(z_m)} \sqrt{\frac{(z - \hat{y})^T (z - \hat{y})}{N}} \tag{24}$$

where $\hat{y}$ is the length N time-domain model output and z is the length N time-domain measured output. The range of response values used to develop the model [range$(z_m) = \max(z_m) - \min(z_m)$] serves as the error normalization metric for the NRMSE computed for both modeling and validation data. The NRMSE values for each reference flight condition are compared in Fig. 16. The associated modeling and validation NRMSE values for each local model are similar and low-valued indicating that the identified models have good prediction capability across the flight envelope.

Figure 17 shows the variation of the final dynamic derivative estimates across the tested freestream airspeed conditions. These high-fidelity aero-propulsive damping estimates are the main aerodynamic information desired from 3DOF wind-tunnel experiments. After the 3DOF wind-tunnel testing and modeling efforts were completed, the identified dynamic derivative estimates were incorporated into the RAVEN-SWFT flight dynamics simulation described in Sec. IV.A and used alongside the static aero-propulsive model created from previous wind-tunnel testing. The new high-fidelity damping estimates extracted from 3DOF wind-tunnel testing improved the RAVEN-SWFT flight simulation in dynamic maneuvering and the model-based FCS design that will be used in future flight testing.
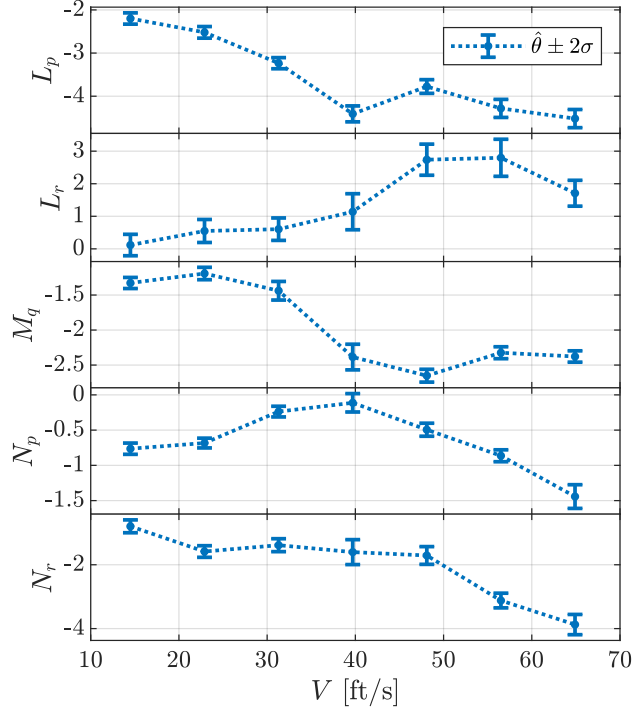
Fig. 17 Variation of RAVEN-SWFT dynamic derivative estimates with freestream airspeed.

IX. Discussion

The preceding results show that accurate aero-propulsive damping estimates have been identified for the RAVEN-SWFT vehicle using the 3DOF free motion testing and modeling approach developed in this paper. Furthermore, after vehicle installation and FCS evaluation, the models at each reference flight condition were developed using under 10 minutes of wind-on test execution time, with even less time needed to collect the minimum required data to develop an accurate model. When applying the test technique and modeling approach to develop damping estimates across the transition envelope, a global aero-propulsive damping model can be developed using only hours of wind-tunnel test time. This approach is significantly faster than traditional forced oscillation wind-tunnel testing, where multiple single-frequency sinusoid forced motion maneuvers are conducted separately for the roll, pitch, and yaw degrees of freedom at each flight condition.

When using the modeling approach developed in this work, a few limitations and drawbacks should be considered relative to forced oscillation experiments. First, the models are based on a quasi-steady assumption, where aero-propulsive effects at the current point in time are only dependent on the current states and controls. Conversely, forced oscillation experiments readily allow for characterization of unsteady aerodynamics (e.g., see Ref. [22]). Second, since the 3DOF apparatus currently lacks a force measurement capability, damping effects could only be identified in the aero-propulsive moments, whereas forced oscillation experiments use a balance allowing for determination of damping effects in both the applied forces and moments. Although, because the dominant aerodynamic damping effects appear in the moments, this is not considered to be a major limitation. Future 3DOF experiments may incorporate a force measurement device to allow for damping characterization in both the forces and moments. Third, in order to conduct 3DOF wind-tunnel testing, a vehicle FCS must be developed and integrated to regulate vehicle motion and inject PTIs, which is a major engineering development effort. Finally, the vehicle moments of inertia must be accurately determined prior to conducting 3DOF testing, requiring significant engineering effort, to calculate the aero-propulsive moment response variables. Neither development of a control system nor determination of vehicle moments of inertia are required to conduct forced oscillation wind-tunnel testing.

Although it is not the focus of this paper, the flight control software development process also substantially benefits from performing 3DOF wind-tunnel testing. Flight testing of new experimental flight control software must proceed very cautiously because of the elevated risk posed to the vehicle. Therefore, substantial effort is invested in performing flight simulations and hardware-in-the-loop bench testing before flight testing new control software. However, because

of differences in the simulation and hardware-in-the-loop environment compared to flight, these software verification efforts can fail to identify possible issues that arise when operating onboard a vehicle in a flight-test environment, which can lead to expensive, unforeseen project delays. 3DOF wind-tunnel testing allows the vehicle to be flown in multiple rotational degrees of freedom in a flight-like environment, while posing little risk to the vehicle, similar to bench testing. The 3DOF test capability allows the flight control software to be efficiently and rigorously tested, while also permitting rapid implementation and testing of software changes based on observations from testing. For RAVEN-SWFT, the custom FCS was able to be rigorously tested and refined on the 3DOF rig through most of the transition envelope using nearly the same hardware and flight control software (excluding the outer-loop control laws) that will be used in upcoming flight testing. In addition to aero-propulsive damping characterization, flight control software verification formed a major aspect of the RAVEN-SWFT 3DOF wind-tunnel testing, which accelerated flight control software development and served as a flight-test risk reduction effort enabled by the 3DOF test capability.

X. Conclusions

Accurate and efficient modeling of eVTOL aircraft is essential for numerous activities required to enable safe and effective eVTOL aircraft flight operations. Static wind-tunnel testing is a common way to characterize the static aircraft aerodynamics and control effectiveness. Dynamic wind-tunnel testing, such as forced oscillation testing, allows for accurate determination of aerodynamic damping effects that are important to include in flight dynamics simulations, but is a time consuming and specialized endeavor even for simple aircraft configurations. For eVTOL aircraft that have many control effectors, substantial aero-propulsive coupling, and many operational flight conditions, full-envelope forced oscillation testing is impractical to efficiently accomplish.

This paper presented a new 3DOF free motion wind-tunnel testing and model identification strategy for eVTOL aircraft aero-propulsive modeling to support flight dynamics simulation development. The approach was applied to the RAVEN-SWFT subscale tiltrotor eVTOL aircraft, which exhibits complexity representative of many current and future eVTOL aircraft configurations. A custom flight control system was developed and deployed onto the vehicle for free motion testing to stabilize the aircraft and track attitude commands. While the flight controller was active, orthogonal phase-optimized multisine PTI excitations were injected into the attitude and control effector commands to perturb the aircraft around the reference condition and collect information-rich data for modeling. The multiple-input experiment design simultaneously excites the aircraft in all axes, resulting in very efficient testing. Five or more 60-seconds multisine maneuvers were collected at seven different nonzero airspeed conditions in the RAVEN-SWFT transition envelope. The wind-tunnel data collection time was substantially lower than equivalent forced oscillation testing, while still providing data enabling accurate characterization of the dominant aero-propulsive damping effects exerted on the vehicle. Model parameters in a mostly linear aero-propulsive model structure were determined at each different reference flight condition in the RAVEN-SWFT transition envelope. Parameter estimation was performed using the equation-error method in the frequency domain. The identified models were shown to have good predictive capability and small normalized model fit error. The accurate dynamic derivatives identified throughout the test envelope were used to improved the RAVEN-SWFT flight dynamics simulation.

Based on the successful modeling results, the presented 3DOF free motion testing and modeling approach is recommended for future dynamic wind-tunnel testing for both conventional and complex aircraft configurations. The method enables development of an accurate aircraft dynamic model using a short amount of wind-tunnel test time, with minimal risk posed to the vehicle. The general approach can be applied to many current and future aeronautical vehicles.

References

[1] Johnson, W., Silva, C., and Solis, E., "Concept Vehicles for VTOL Air Taxi Operations," *AHS Technical Conference on Aeromechanics Design for Transformative Vertical Flight*, Jan. 2018.

[2] Silva, C., Johnson, W., Antcliff, K. R., and Patterson, M. D., "VTOL Urban Air Mobility Concept Vehicles for Technology Development," *2018 Aviation Technology, Integration, and Operations Conference*, AIAA Paper 2018-3847, Jun. 2018. https://doi.org/10.2514/6.2018-3847.

[3] Saeed, A. S., Younes, A. B., Cai, C., and Cai, G., "A Survey of Hybrid Unmanned Aerial Vehicles," *Progress in Aerospace Sciences*, Vol. 98, 2018, pp. 91–105. https://doi.org/10.1016/j.paerosci.2018.03.007.

[4] Kim, H. D., Perry, A. T., and Ansell, P. J., "A Review of Distributed Electric Propulsion Concepts for Air Vehicle Technology," *2018 AIAA/IEEE Electric Aircraft Technologies Symposium*, AIAA Paper 2018-4998, Jul. 2018. https://doi.org/10.2514/6.2018-4998.

[5] Johnson, W., and Silva, C., "NASA Concept Vehicles and the Engineering of Advanced Air Mobility Aircraft," *The Aeronautical Journal*, Vol. 126, No. 1295, 2022, pp. 59–91. https://doi.org/10.1017/aer.2021.92.

[6] "eVTOL Aircraft Directory," *Electric VTOL News™*, https://evtol.news/aircraft, Accessed 20 November 2024.

[7] Busan, R. C., Rothhaar, P. M., Croom, M. A., Murphy, P. C., Grafton, S. B., and O'Neal, A. W., "Enabling Advanced Wind-Tunnel Research Methods Using the NASA Langley 12-Foot Low Speed Tunnel," *14th AIAA Aviation Technology, Integration, and Operations Conference*, AIAA Paper 2014-3000, Jun. 2014. https://doi.org/10.2514/6.2014-3000.

[8] Murphy, P. C., and Landman, D., "Experiment Design for Complex VTOL Aircraft with Distributed Propulsion and Tilt Wing," *AIAA Atmospheric Flight Mechanics Conference*, AIAA Paper 2015-0017, Jan. 2015. https://doi.org/10.2514/6.2015-0017.

[9] Busan, R. C., Murphy, P. C., Hatke, D. B., and Simmons, B. M., "Wind Tunnel Testing Techniques for a Tandem Tilt-Wing, Distributed Electric Propulsion VTOL Aircraft," *AIAA SciTech 2021 Forum*, AIAA Paper 2021-1189, Jan. 2021. https://doi.org/10.2514/6.2021-1189.

[10] Simmons, B. M., and Murphy, P. C., "Aero-Propulsive Modeling for Tilt-Wing, Distributed Propulsion Aircraft Using Wind Tunnel Data," *Journal of Aircraft*, Vol. 59, No. 5, 2022, pp. 1162–1178. https://doi.org/10.2514/1.C036351.

[11] Simmons, B. M., Morelli, E. A., Busan, R. C., Hatke, D. B., and O'Neal, A. W., "Aero-Propulsive Modeling for eVTOL Aircraft Using Wind Tunnel Testing with Multisine Inputs," *AIAA AVIATION 2022 Forum*, AIAA Paper 2022-3603, Jun. 2022. https://doi.org/10.2514/6.2022-3603.

[12] Simmons, B. M., and Busan, R. C., "Statistical Wind-Tunnel Experimentation Advancements for eVTOL Aircraft Aero-Propulsive Model Development," *AIAA SciTech 2024 Forum*, AIAA Paper 2024-2482, Jan. 2024. https://doi.org/10.2514/6.2024-2482.

[13] Murphy, P. C., Buning, P. G., and Simmons, B. M., "Rapid Aero Modeling for Urban Air Mobility Aircraft in Computational Experiments," *AIAA SciTech 2021 Forum*, AIAA Paper 2021-1002, Jan. 2021. https://doi.org/10.2514/6.2021-1002.

[14] Simmons, B. M., Buning, P. G., and Murphy, P. C., "Full-Envelope Aero-Propulsive Model Identification for Lift+Cruise Aircraft Using Computational Experiments," *AIAA AVIATION 2021 Forum*, AIAA Paper 2021-3170, Aug. 2021. https://doi.org/10.2514/6.2021-3170.

[15] Simmons, B. M., "System Identification Approach for eVTOL Aircraft Demonstrated Using Simulated Flight Data," *Journal of Aircraft*, Vol. 60, No. 4, 2023, pp. 1078–1093. https://doi.org/10.2514/1.C036896.

[16] Morelli, E. A., and Klein, V., *Aircraft System Identification: Theory and Practice*, 2nd ed., Sunflyte Enterprises, Williamsburg, VA, 2016.

[17] Jategaonkar, R. V., *Flight Vehicle System Identification: A Time-Domain Methodology*, 2nd ed., American Institute of Aeronautics and Astronautics, Reston, VA, 2015. https://doi.org/10.2514/4.102790.

[18] Tischler, M. B., and Remple, R. K., *Aircraft and Rotorcraft System Identification: Engineering Methods With Flight-Test Examples*, 2nd ed., American Institute of Aeronautics and Astronautics, Reston, VA, 2012. https://doi.org/10.2514/4.868207.

[19] Geuther, S. C., North, D. D., and Busan, R. C., "Investigation of a Tandem Tilt-wing VTOL Aircraft in the NASA Langley 12-Foot Low-Speed Tunnel," NASA TM–2020–5003178, Jun. 2020.

[20] Owens, B., Brandon, J., Croom, M., Fremaux, M., Heim, G., and Vicroy, D., "Overview of Dynamic Test Techniques for Flight Dynamics Research at NASA LaRC," *25th AIAA Aerodynamic Measurement Technology and Ground Testing Conference*, AIAA Paper 2006-3146, June 2006. https://doi.org/10.2514/6.2006-3146.

[21] Vicroy, D. D., Loeser, T. D., and Schütte, A., "Static and Forced-Oscillation Tests of a Generic Unmanned Combat Air Vehicle," *Journal of Aircraft*, Vol. 49, No. 6, 2012, pp. 1558–1583. https://doi.org/10.2514/1.C031501.

[22] Murphy, P. C., Klein, V., and Frink, N. T., "Nonlinear Unsteady Aerodynamic Modeling Using Wind-Tunnel and Computational Data," *Journal of Aircraft*, Vol. 54, No. 2, 2017, pp. 659–683. https://doi.org/10.2514/1.C033881.

[23] Vicroy, D. D., "A Guide to Forced Oscillation Data Processing and Analysis," NASA TP–20210023569, Jun. 2023.

[24] Huang, M., and Wang, Z.-w., "A Review of Wind Tunnel Based Virtual Flight Testing Techniques for Evaluation of Flight Control Systems," *International Journal of Aerospace Engineering*, 2015, pp. 1–22. https://doi.org/10.1155/2015/672423.

[25] Rajamurthy, M. S., "Generation of Comprehensive Longitudinal Aerodynamic Data Using Dynamic Wind-Tunnel Simulation," *Journal of Aircraft*, Vol. 34, No. 1, 1997, pp. 29–33. https://doi.org/10.2514/2.2157.

[26] Davison, P. M., Lowenberg, M. H., and Di Bernardo, M., "Experimental Analysis and Modeling of Limit Cycles in a Dynamic Wind-Tunnel Rig," *Journal of Aircraft*, Vol. 40, No. 4, 2003, pp. 776–785. https://doi.org/10.2514/2.3158.

[27] Capone, F. J., Owens, D. B., and Hall, R. M., "Development of a Transonic Free-To-Roll Test Capability," *Journal of Aircraft*, Vol. 41, No. 3, 2004, pp. 456–463. https://doi.org/10.2514/1.1449.

[28] Owens, D. B., McConnell, J. K., Brandon, J. M., and Hall, R. M., "Transonic Free-To-Roll Analysis of the F-35 (Joint Strike Fighter) Aircraft," *Journal of Aircraft*, Vol. 43, No. 3, 2006, pp. 608–615. https://doi.org/10.2514/1.16972.

[29] Tang, D., and Dowell, E. H., "Effects of a Free-to-Roll Fuselage on Wing Flutter: Theory and Experiment," *AIAA Journal*, Vol. 52, No. 12, 2014, pp. 2625–2632. https://doi.org/10.2514/1.J052562.

[30] Gatto, A., "Application of a Pendulum Support Test Rig for Aircraft Stability Derivative Estimation," *Journal of Aircraft*, Vol. 46, No. 3, 2009, pp. 927–934. https://doi.org/10.2514/1.38916.

[31] Navaratna, P. D. B., Lowenberg, M. H., Neild, S. A., and Goman, M., "Self-Induced Roll–Yaw Oscillations of an Aircraft Model in a Wind Tunnel," *Journal of Aircraft*, Vol. 59, No. 1, 2022, pp. 3–14. https://doi.org/10.2514/1.C036157.

[32] Papageorgiou, G., and Glover, K., "Two-Degree-of-Freedom Control of an Actively Controlled Wind-Tunnel Model," *Journal of Guidance, Control, and Dynamics*, Vol. 25, No. 3, 2002, pp. 510–516. https://doi.org/10.2514/2.4911.

[33] Gatto, A., and Lowenberg, M. H., "Evaluation of a Three Degree of Freedom Test Rig for Stability Derivative Estimation," *Journal of Aircraft*, Vol. 43, No. 6, 2006, pp. 1747–1761. https://doi.org/10.2514/1.19821.

[34] Ignatyev, D. I., Sidoryuk, M. E., Kolinko, K. A., and Khrabrov, A. N., "Dynamic Rig for Validation of Control Algorithms at High Angles of Attack," *Journal of Aircraft*, Vol. 54, No. 5, 2017, pp. 1760–1771. https://doi.org/10.2514/1.C034167.

[35] Cook, M., "On the Use of Small Scale Aircraft Models for Dynamic Wind Tunnel Investigation of Stability and Control," *Transactions of the Institute of Measurement and Control*, Vol. 9, No. 4, 1987, pp. 190–197. https://doi.org/10.1177/014233128700900405.

[36] Carnduff, S. D., Erbsloeh, S. D., Cooke, A. K., and Cook, M. V., "Characterizing Stability and Control of Subscale Aircraft from Wind-Tunnel Dynamic Motion," *Journal of Aircraft*, Vol. 46, No. 1, 2009, pp. 137–147. https://doi.org/10.2514/1.36730.

[37] Pattinson, J., Lowenberg, M. H., and Goman, M. G., "Multi-Degree-of-Freedom Wind-Tunnel Maneuver Rig for Dynamic Simulation and Aerodynamic Model Identification," *Journal of Aircraft*, Vol. 50, No. 2, 2013, pp. 551–566. https://doi.org/10.2514/1.C031924.

[38] Pattinson, J., Lowenberg, M. H., and Goman, M. G., "Investigation of Poststall Pitch Oscillations of an Aircraft Wind-Tunnel Model," *Journal of Aircraft*, Vol. 50, No. 6, 2013, pp. 1843–1855. https://doi.org/10.2514/1.C032184.

[39] Gong, Z., Araujo-Estrada, S., Lowenberg, M. H., Neild, S. A., and Goman, M. G., "Experimental Investigation of Aerodynamic Hysteresis Using a Five-Degree-of-Freedom Wind-Tunnel Maneuver Rig," *Journal of Aircraft*, Vol. 56, No. 3, 2019, pp. 1029–1039. https://doi.org/10.2514/1.C034995.

[40] "System IDentification Programs for AirCraft (SIDPAC)," *NASA Technology Transfer Program*, https://software.nasa.gov/software/LAR-16100-1, Accessed 08 November 2024.

[41] Geuther, S. C., Simmons, B. M., and Ackerman, K. A., "Overview of the Subscale RAVEN Flight Controls and Modeling Testbed," *Vertical Flight Society's 80th Annual Forum & Technology Display*, May 2024.

[42] German, B. J., Jha, A., Whiteside, S. K. S., and Welstead, J. R., "Overview of the Research Aircraft for eVTOL Enabling techNologies (RAVEN) Activity," *AIAA AVIATION 2023 Forum*, AIAA Paper 2023-3924, June 2023. https://doi.org/10.2514/6.2023-3924.

[43] "NASA Langley 12-Foot Low-Speed Tunnel," https://researchdirectorate.larc.nasa.gov/12-foot-low-speed-tunnel-12-ft-lst/, Accessed 08 November 2024.

[44] McSwain, R. G., Geuther, S. C., Howland, G., Patterson, M. D., Whiteside, S. K., and North, D. D., "An Experimental Approach to a Rapid Propulsion and Aeronautics Concepts Testbed," NASA TM–2020-220437, Jan. 2020.

[45] North, D. D., Busan, R. C., and Howland, G., "Design and Fabrication of the Langley Aerodrome No. 8 Distributed Electric Propulsion VTOL Testbed," *AIAA SciTech 2021 Forum*, AIAA Paper 2021-1188, Jan. 2021. https://doi.org/10.2514/6.2021-1188.

[46] Rothhaar, P. M., Murphy, P. C., Bacon, B. J., Gregory, I. M., Grauer, J. A., Busan, R. C., and Croom, M. A., "NASA Langley Distributed Propulsion VTOL Tilt-Wing Aircraft Testing, Modeling, Simulation, Control, and Flight Test Development," *14th AIAA Aviation Technology, Integration, and Operations Conference*, AIAA Paper 2014-2999, Jun. 2014. https://doi.org/10.2514/6.2014-2999.

[47] Geuther, S. C., and Fei, X., "LA-8 Computational Analysis and Validation Studies Using FlightStream," *AIAA SciTech 2021 Forum*, AIAA Paper 2021-1191, Jan. 2021. https://doi.org/10.2514/6.2021-1191.

[48] Ahuja, V., and Hartfield, R. J., "Reduced-Order Aerodynamics with the Method of Integrated Circulation," *AIAA SciTech 2022 Forum*, AIAA Paper 2022-0005, Jan. 2022. https://doi.org/10.2514/6.2022-0005.

[49] Simmons, B. M., Geuther, S., and Ahuja, V., "Validation of a Mid-Fidelity Approach for Aircraft Stability and Control Characterization," *AIAA AVIATION 2023 Forum*, AIAA Paper 2023-4076, Jun. 2023. https://doi.org/10.2514/6.2023-4076.

[50] DiMaggio, G. A., Simmons, B. M., Geuther, S. C., Hartfield Jr., R. J., and Ahuja, V., "Transition Aero-Propulsive Analysis of a Tilt-Wing eVTOL Aircraft Using a Surface-Vorticity Solver," *AIAA SciTech 2025 Forum*, Jan. 2025. To be published.

[51] Simmons, B. M., "System Identification for Propellers at High Incidence Angles," *Journal of Aircraft*, Vol. 58, No. 6, 2021, pp. 1336–1350. https://doi.org/10.2514/1.C036329.

[52] Simmons, B. M., and Hatke, D. B., "Investigation of High Incidence Angle Propeller Aerodynamics for Subscale eVTOL Aircraft," NASA TM–20210014010, May 2021.

[53] Stratton, M., and Landman, D., "Wind Tunnel Test and Empirical Modeling of Tilt-Rotor Performance for eVTOL Applications," *AIAA SciTech 2021 Forum*, AIAA Paper 2021-0834, Jan. 2021. https://doi.org/10.2514/6.2021-0834.

[54] Simmons, B. M., "Evaluation of Response Surface Experiment Designs for Distributed Propulsion Aircraft Aero-Propulsive Modeling," *AIAA SciTech 2023 Forum*, AIAA Paper 2023-2251, Jan. 2023. https://doi.org/10.2514/6.2023-2251.

[55] Cooper, J. R., Ackerman, K. A., Rothhaar, P. M., and Gregory, I. M., "Autonomous Path-Following for a Tilt-Wing, Distributed Electric Propulsion, Vertical Take-Off and Landing Unmanned Aerial System in Hover Mode," NASA TM–2018–220109, Nov. 2018.

[56] Cook, J., and Gregory, I., "A Robust Uniform Control Approach for VTOL Aircraft," *VFS Autonomous VTOL Technical Meeting and Electric VTOL Symposium*, Jan. 2021.

[57] McSwain, R. G., Glaab, L. J., and Theodore, C. R., "Greased Lightning (GL-10) Performance Flight Research – Flight Data Report," NASA TM–2017–219794, Nov. 2017.

[58] Fredericks, W. J., McSwain, R. G., Beaton, B. F., Klassman, D. W., and Theodore, C. R., "Greased Lightning (GL-10) Flight Testing Campaign," NASA TM–2017–219643, Jul. 2017.

[59] Simmons, B. M., "Efficient Variable-Pitch Propeller Aerodynamic Model Development for Vectored-Thrust eVTOL Aircraft," *AIAA AVIATION 2022 Forum*, AIAA Paper 2022-3817, Jun. 2022. https://doi.org/10.2514/6.2022-3817.

[60] Montgomery, D. C., *Design And Analysis of Experiments*, 8th ed., John Wiley & Sons, Inc., Hoboken, NJ, 2013.

[61] Myers, R. H., Montgomery, D. C., and Anderson-Cook, C. M., *Response Surface Methodology: Process and Product Optimization Using Designed Experiments*, 4th ed., John Wiley & Sons, 2016.

[62] Fritsch, F. N., and Carlson, R. E., "Monotone Piecewise Cubic Interpolation," *SIAM Journal on Numerical Analysis*, Vol. 17, No. 2, 1980, pp. 238–246. https://doi.org/10.1137/0717021.

[63] Moler, C. B., *Numerical Computing with MATLAB*, Society for Industrial and Applied Mathematics, Philadelphia, PA, 2004. https://doi.org/10.1137/1.9780898717952.

[64] "FlightStream®," *Research in Flight*, https://researchinflight.com/, Accessed 08 November 2024.

[65] "Flight Dynamics Simulation of a Generic Transport Model," NASA Technology Transfer Program, https://software.nasa.gov/software/LAR-17625-1, Accessed 26 March 2024.

[66] Etkin, B., and Reid, L. D., *Dynamics of Flight: Stability and Control*, 3rd ed., John Wiley & Sons, Inc, New York, NY, 1996.

[67] Stevens, B. L., Lewis, F. L., and Johnson, E. N., *Aircraft Control and Simulation: Dynamics, Controls Design, and Autonomous Systems*, 3rd ed., John Wiley & Sons, Hoboken, NJ, 2015.

[68] Chen, C.-T., *Linear System Theory and Design*, 4th ed., Oxford University Press, 2014.

[69] Lavretsky, E., and Wise, K. A., *Robust and Adaptive Control: With Aerospace Applications*, 2nd ed., Springer, Cham, Switzerland, 2024.

[70] "MathWorks Documentation," https://www.mathworks.com/help/, Accessed 29 April 2024.

[71] Asper, G. D., and Simmons, B. M., "Rapid Flight Control Law Deployment and Testing Framework for Subscale VTOL Aircraft," NASA TM–20220011570, Sep. 2022.

[72] Asper, G. D., Simmons, B. M., Axten, R. M., Ackerman, K. A., and Corrigan, P. E., "Inexpensive Multirotor Platform for Advanced Controls Testing (IMPACT): Development, Integration, and Experimentation," NASA TM–20240000223, Mar. 2024.

[73] Morelli, E. A., "Multiple Input Design for Real-Time Parameter Estimation in the Frequency Domain," *13th IFAC Conference on System Identification*, Aug. 2003. https://doi.org/10.1016/S1474-6670(17)34833-4.

[74] Morelli, E. A., "Flight-Test Experiment Design for Characterizing Stability and Control of Hypersonic Vehicles," *Journal of Guidance, Control, and Dynamics*, Vol. 32, No. 3, 2009, pp. 949–959. https://doi.org/10.2514/1.37092.

[75] Morelli, E. A., "Practical Aspects of Multiple-Input Design for Aircraft System Identification Flight Tests," *AIAA AVIATION 2021 Forum*, AIAA Paper 2021-2795, Aug. 2021. https://doi.org/10.2514/6.2021-2795.

[76] Grauer, J. A., and Boucher, M., "System Identification of Flexible Aircraft: Lessons Learned from the X-56A Phase 1 Flight Tests," *AIAA SciTech 2020 Forum*, AIAA Paper 2020-1017, Jan. 2020. https://doi.org/10.2514/6.2020-1017.

[77] Fremaux, C. M., Simmons, B. M., Owens, D. B., Vicroy, D. D., and Storch, D. B., "Development and Capabilities of the NASA Flight Dynamics Research Facility," *AIAA SciTech 2025 Forum*, Jan. 2025. To be published.

[78] Morelli, E. A., "Practical Aspects of the Equation-Error Method for Aircraft Parameter Estimation," *AIAA Atmospheric Flight Mechanics Conference and Exhibit*, AIAA Paper 2006-6144, Aug. 2006. https://doi.org/10.2514/6.2006-6144.

[79] Morelli, E. A., and Grauer, J. A., "Practical Aspects of Frequency-Domain Approaches for Aircraft System Identification," *Journal of Aircraft*, Vol. 57, No. 2, 2020, pp. 268–291. https://doi.org/10.2514/1.C035599.

[80] Morelli, E. A., "High Accuracy Evaluation of the Finite Fourier Transform Using Sampled Data," NASA TM-110340, Jun. 1997.

[81] Morelli, E. A., and Klein, V., "Accuracy of Aerodynamic Model Parameters Estimated from Flight Test Data," *Journal of Guidance, Control, and Dynamics*, Vol. 20, No. 1, 1997, pp. 74–80. https://doi.org/10.2514/2.3997.

[82] Klein, V., Batterson, J. G., and Murphy, P. C., "Determination of Airplane Model Structure from Flight Data by Using Modified Stepwise Regression," NASA TP-1916, Oct. 1981.

[83] Montgomery, D. C., Peck, E. A., and Vining, G. G., *Introduction to Linear Regression Analysis*, 5th ed., John Wiley & Sons, Hoboken, New Jersey, 2012.

[84] Young, H. D., *Statistical Treatment of Experimental Data*, McGraw-Hill, New York, 1962. Chapter 4.